Applied Surface Science 609 (2023) 155217

Contents lists available at ScienceDirect

Applied Surface Science

journal homepage: www.elsevier.com/locate/apsusc

Full Length Article

IR nanospectroscopy to decipher drug/metal nanoparticle interactions: Towards a better understanding of the spectral signal enhancement and its distribution

Natalia Piergies [a,*], Jérémie Mathurin [b], Alexandre Dazzi [b], Ariane Deniset-Besseau [b], Magdalena Oćwieja [c], Czesława Paluszkiewicz [a], Wojciech M. Kwiatek [a]

[a] Institute of Nuclear Physics Polish Academy of Sciences, PL-31342 Krakow, Poland
[b] Institut de Chimie Physique, UMR8000, Université Paris-Saclay, CNRS, 91405 Orsay, France
[c] Jerzy Haber Institute of Catalysis and Surface Chemistry Polish Academy of Sciences, Niezapominajek 8, PL-30239 Krakow, Poland

ARTICLE INFO

Keywords:
Gefitinib
Drug's adsorption
Metal nanoparticle mono-layer
Infrared nanospectroscopy
surface-enhanced Raman spectroscopy (SERS)

ABSTRACT

In this study, detailed considerations of the interactions appearing at drug/metal nanoparticle interfaces in micro- and nanoscale were performed. Application of the well-known surface-enhanced Raman spectroscopy (SERS) reveals information of how gefitinib, a drug approved in non-small cell lung cancer therapy, connects to the silver and gold nanoparticles (AgNPs and AuNPs, respectively). Such knowledge is important in the context of using the resulting conjugates to increase the effectiveness of cancer therapy. The received data were extended by the nanoscale analysis using atomic force microscopy in combination with the surface-enhanced infrared spectroscopy (AFM-SEIRA) in tapping mode. This allows to better visualize the discussed interaction with ultra-high spatial resolution even reaching the size of the particular nanoparticle (~15 nm). It should be noted, that the metal nanoparticle mono-layer was enough to enhance the obtained AFM-SEIRA signal, which for the conventional surface-enhanced vibrational techniques would be unattainable. Moreover, since the surface enhancement phenomenon observed in the AFM-SEIRA technique is not fully understood the comparison between this effect and the signal reinforcement in SERS was performed. The drawn conclusions suggest the complementarity of both applied techniques and try to prove the statement that the intensity AFM-SEIRA maps reveal the nature of the drug/metal nanostructure interaction.

1. Introduction

Nowadays, the development of advanced methods ensuring insights into the nanochemical properties and information of investigated species is highly desirable [1–4]. Such a scientific approach allows for exploring new materials or performing detailed characterization of well-known objects, which often leads to new groundbreaking conclusions [5–8]. This progression has been possible based on the near-field spectroscopic methods which combine the atomic force microscopy (AFM) with infrared (IR) and Raman (RS) spectroscopies. However, the application of such methods as IR scattering scanning nearfield optical microscopy (IR-sSNOM) [9,10] and tip-enhanced Raman spectroscopy (TERS) [11,12] requires appropriate experience and focusing on the critical paths during the experiments. One of the main issues is associated with the specially prepared probes which determine the signal enhancement, contrast of the obtained results, and tip-sample interaction [13,14]. The latter is especially important for the reproducibility of the results [14–16]. Therefore, optimization of the experiment at every stage is crucial and requires a good understanding of the phenomena that govern signal detection for the particular near-field methods.

In light of the foregoing considerations, the AFM-IR technique which combines atomic force microscopy (AFM) with IR spectroscopy appears to be a more sufficient tool for imaging and chemical characterization for various types of samples providing more repeatable data [5,6,17–24]. Based on the thermal expansion phenomenon induced by the molecular absorption of the IR radiation this technique uses an AFM probe as a signal detector and thus allows to circumvent the diffraction limit. Therefore, the spatial resolution for this technique is limited only by the tip radius what is practically below 20 nm [25]. The relevance of the AFM-IR technique relies in the assumption that the absorption coefficient of the sample is directly proportional to the thermal expansion

* Corresponding author.

https://doi.org/10.1016/j.apsusc.2022.155217
Received 25 July 2022; Received in revised form 26 September 2022; Accepted 3 October 2022
Available online 17 October 2022

appearing within this sample [1,26]. Consequently, the recorded signal correlates very well with the one obtained using conventional far-field IR spectroscopy. The ultra-high-resolution together with the not-so-complex phenomenon which does not require long-term optimization of the measurement gives the possibility of the AFM-IR technique becoming an excellent tool for routine analytical studies.

Since the surface enhancement effect occurring in the surface-enhanced infrared absorption spectroscopy (SEIRA) also has been proved for AFM-IR, this technique has been successfully used for the interpretation of how the molecules adsorb on the metal layers giving sub-molecular information about the interaction at the molecule/metal interface [24,27,28]. Previously, we presented the AFM-IR investigations of erlotinib (a drug approved in non-small cell lung cancer therapy) immobilized on mono-layers of the 15 nm silver and gold nanoparticles (AgNPs and AuNPs, respectively) [29]. Application of the surface selection rules typical for the SEIRA technique [30–32] gave an insight into the induced connection between the drug and the metal mono-layer at the single nanoparticle resolution level. It should be noted that the characterization of erlotinib-loaded nanoparticle systems obtained using AFM-IR corresponds very well with this received from the surface-enhanced Raman spectroscopy (SERS) technique [28,33,34]. Additionally, for the first time we have shown the unique visualization of the spectral signal of the drug on the metal mono-layer using the tapping AFM-IR technique [29]. As it was mentioned above, the surface enhancement effect applied for the extreme signal amplification in SEIRA is also observed for the AFM-IR technique. Such enhancement is associated with the localized plasmon resonance of metal nanostructures induced by incoming radiation. This resonance generates a huge local electromagnetic field which is much stronger than the energy from the incident photons [35,36]. As a consequence, characteristic areas on the metal with enormous enhanced optical fields called “hot spots” [37–39] appear. The localization of those regions is strongly related to the structure and morphology of the metal. Considering the spherical nanoparticles (NPs), which are commonly known as active substrates for the SEIRA and SERS techniques, the reinforced electromagnetic field occurs between the particular spheres [40]. One of the conditions that must be satisfied is an appropriate relatively small distance between the nanospheres of the created mono-layer (less than twice the nanoparticle diameter for SERS and less than 5 nm for SEIRA) [41,42]. Based on this, the tapping AFM-IR maps for a molecule immobilized on the metal surface should be characteristic of the distribution of its spectral signal related to the areas with the strongest electromagnetic field enhancement namely “hot spots”. However, the recorded data for erlotinib deposited on the AgNP and AuNP mono-layers, respectively, indicate ambiguous results [29]. The image of the signal distribution on the AgNP mono-layer corresponds very well with the “hot spot” theory that is the most intense signal that appears between particular nanospheres on the considered mono-layer. However, the signal repartition for the AuNP mono-layer was not so homogenous and some strong enhancement are also present on top of NPs. These noticed discrepancies prompt us to extend our research to better understand the surface enhancement effect and its contribution to the AFM-IR spectra and maps for molecules deposited on the metal NP mono-layers.

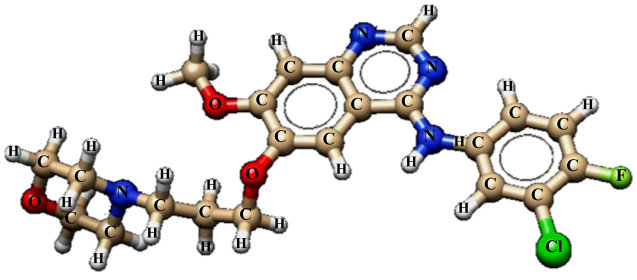

Fig. 1. Molecular structure of gefitinib.

The main goal of this study was to characterize how gefitinib (see Fig. 1 for the molecular structure), a drug approved in the targeted therapy for non-small cell lung cancer, adsorbs on the AgNP and AuNP mono-layers, respectively using the tapping AFM-IR technique.

Alone the gefitinib should be used at high dose to obtain an effective therapeutic response. As a consequence, several side effects are observed for this treatment such as nausea, vomiting, rash, diarrhea, and in sporadic cases progression of interstitial lung disease. The improvement of the drug delivery and bioavailability within the organ is essential [43]. The introduction of the stable drug/nanocarrier systems into cancer therapy might improve this bioavailability and decrease the drug concentration necessary for the better treatment response. To increase the bioavailability of the drug, our strategy is to associate it with biocompatible metal NPs. The elucidation of how gefitinib connects to those metal NPs and deep analysis of the gefitinib/nanoparticle conjugates is especially important in relation to the development of an effective drug delivery system.

We propose to use the AFM-IR technique for the visualization of how gefitinib adsorbs on the two different types of metal mono-layers. We expect it will allow a deep investigation of the surface phenomenon appearing during the signal reinforcement obtained from the application of the metal mono-layer. Additionally, as the surface enhancement effect in photothermal technique, AFM-IR, is not fully understood, this issue has also been considered. Furthermore, to verify the gefitinib interaction with the metal NPs and the interpretation of the enhancement obtained with the AFM-IR system, the same gefitinib/NPs systems was also explored by SERS. To the best of our knowledge, such consideration has not been reported.

2. Experimental

2.1. Materials

Silver nitrate, tetrachloroauricacid acid, trisodium citrate dihydrate, sodium borohydride, sodium chloride, sodium hydroxide, and hydrochloric acid used in the experiments were commercial products of Sigma Aldrich. These chemicals were used without further purification. Ultrapure water (Milli-Q water) applied for the preparation of aqueous solutions was obtained with the use of a Milli-Q Elix& Simplicity 185 purification system (Millipore SA, Molsheim, France).

2.2. Plasmonic nanoparticle preparation

Citrate-stabilized AgNPs were prepared according to the modified Lee and Meisel procedure (Lee and Meisel) [44]. Briefly, 15 mg sodium borohydride was dissolved in 500 mL of 45 mM aqueous solution of trisodium citrate. Then, under ambient conditions and vigorous stirring (170 rpm) 250 mL of 1 mM silver nitrate was added dropwise (12.5 mL/min) into the previously prepared reduction mixture. After, the end of the addition of silver nitrate, the mixing of newly formed AgNP suspension was proceed for 1 h.

Citrate-stabilized AuNPs were synthesized based on the protocols developed by Turkevic [45,46] and Frens [47]. For this purpose, 250 mL of 1.5 mM hydrogen tetrachloroaurate aqueous solution was heated up to 90 °C under a reflux condenser. Then, 15 mL of 45 mM trisodium citrate aqueous solution was introduced dropwise (1.5 mL/min) to the gold precursor. The reaction mixture was maintained under heating and vigorous mixing (170 rpm) for 30 min. Then, the prepared AuNP suspension was cooled down on the ice bath to room temperature. Both suspensions were purified from the excess of stabilizing agent molecules and other electrolytes used during the preparation procedures. The purification procedure was carried out in an Amicone Filtration cell (model 8400) using membranes made of regenerated cellulose. The suspensions were washed with Milli-Q water until the conductivity of the effluents attained the value of 20 μS/cm. It was established that after the purification process pH of the suspensions varied between 5.8 and

6.4.

The mass concentration of NPs in the purified suspensions was determined based on the density measurements of suspensions and effluents collected during the washing procedure. Knowing these values, the specific density of silver (10.49 g cm^{-3}) and gold (19.3 g cm^{-3}) as well as applying the protocol described previously [48], it was found that the concentration of AgNPs and AuNPs was equal to 124 mg/L and 138 mg/L, respectively. The optical properties of AgNPs and AuNPs dispersed in the suspensions of controlled pH, ionic strength, and temperature were investigated using a UV-2600 spectrometer (Shimadzu, Kyoto, Japan). It was established that the maximum adsorption band of AgNPs appears at a wavelength of 396 nm whereas for the AuNPs it was detected at 521 nm (Supplementary material, Fig. S1). The morphology, size distribution, and average size of both types of plasmonic NPs were determined using micrographs recorded using an JEOL JSM-7500F electron microscope working in the transmission mode (TEM). The analysis of TEM micrographs with the use of MultiScan software (Computer scanning system) enables to establish that the NPs exhibited quasi-spherical shape and a rather narrow size distribution (Supplementary material, Fig. S2). The average size of AgNPs and AuNPs was equal to 12±3 nm and 13±2 nm, respectively.

The stability of AgNPs and AuNPs dispersed in the suspensions of controlled pH, ionic strength, and temperature was evaluated using a Zetasizer Nano ZS instrument (Malvern Instruments, Malvern, UK). The dynamic light scattering (DLS) measurements deliver the information about the diffusion coefficients (hydrodynamic diameter) of NPs whereas the electrophoretic light scattering (ELS) investigations enable to establish the values of electrophoretic mobility (zeta potential) of AgNPs and AuNPs. It was found that both types of NPs were negatively charged in a broad range of pH and ionic strength (Supplementary material, Fig. S3). The zeta potential of AgNPs and AuNPs dispersed in the stock suspension was equal to −67±1 mV and −65±2 mV, respectively. Additionally, it was observed that the zeta potential of NPs was strongly dependent on pH and ionic strength. The decrease of pH and an increase of ionic strength caused the decrease of nanoparticle zeta potential (Supplementary material, Fig. S3). The selected physicochemical properties of AgNPs and AuNPs are provided in Table S1 (Supplementary material).

2.3. Preparation of AgNP and AuNP monolayers on CaF_2 windows

The nanoparticle monolayers of well-controlled coverage and structure were prepared according to the protocol described previously [29]. Briefly, cleaned CaF_2 windows were immersed in an aqueous solution of poly(allylamine hydrochloride) (PAH) of concentration equal to 20 mg/L, ionic strength 0.01 M (regulated by the addition of NaCl) and pH of 5.6. The electrostatically-driven adsorption process of this cationic polyelectrolyte on the surfaces of CaF_2 windows was conducted over 20 min which allowed obtaining a positively charged saturated layer of PAH molecules [49]. After the formation of the supporting layer, the PAH-modified CaF_2 windows were rinsed with Milli-Q water in order to wash unbounded molecules. After the purification positively charged CaF_2 windows were inserted into the stock suspension of AgNPs or AuNPs of ionic strength 0.01 M regulated by the addition of sodium chloride. The diffusion-controlled deposition process of these plasmonic NPs on PAH-modified CaF_2 windows was carried out over 5 h. Then, the samples were gently rinsed with Milli-Q water to remove unbound NPs and excess sodium chloride. Such prepared AgNP and AuNP monolayers were air-dried. The Scheme S1 (Supplementary material) illustrates the various stages of the metal mono-layer preparation. Selected samples were investigated using an JEOL JSM-7500F electron microscope working in the scanning mode (SEM) in order to establish the coverage and structure of formed monolayers. Typically recorded SEM micrographs were presented in the Supplementary material (Fig. S4).

2.4. Sample preparation

The studied drug, gefitinib (*N*-(3-chloro-4-fluoro-phenyl)-7-methoxy-.

6-(3-morpholin-4-ylpropoxy)quinazolin-4-amine; purity 99.75 %), was purchased from Selleckchem company and used without any purification. The drug powder was dissolved in deionized water and the final concentration of the solution was 10^{-3} M. For the SERS experiments, 33 µL of the gefitinib solution was mixed with the 33 µL of the stock suspensions of AgNPs (124 mg/L, pH 6.5) and AuNPs (138 mg/L, pH 5.8) respectively. No additional reagents were added. For the AFM-IR measurements, the same procedure as published before was applied [29]. Briefly, a drop of the drug solution at a concentration of 10^{-3} M was deposited on the CaF_2 window and the appropriate metal mono-layers, respectively, and left to dry. Such an approach gives the possibility to compare the AFM-IR spectra for non-adsorbed and adsorbed gefitinib molecules, thus eliminating an influence of the sample preparation on the obtained results.

2.5. SERS measurements

The SERS spectra for the gefitinib/AgNP and gefitinib/AuNP systems were collected using inVia Renishaw spectrometer combined with a thermoelectrically cooled CCD detector and a Leica confocal microscope with the 20x magnification objective. As excitation sources, the laser lines at 532.0 nm and 632.8 nm, were applied respectively. The application of the two separate laser wavelengths was crucial for optimal signal enhancement since AgNPs and AuNPs possess resonance frequencies in different ranges. For both cases, the three spectra (1 scan with an integration time of 30 s) were recorded in the spectral range of 1800 cm^{-1} – 400 cm^{-1}. The reproducibility of the spectra was confirmed in 3 different regions of the gefitinib/AgNPs and gefitinib/AuNPs, respectively. No changes in the relative intensities of the particular bands in the SERS spectra of the adequate systems were noticed. The decomposition of the sample was no visible in any cases. The corresponding Raman spectra for non-adsorbed gefitinib molecules were recorded using the experimental parameters as it was used for the corresponding SERS experiments.

2.6. Tapping AFM-IR spectroscopy measurements

The AFM-IR spectra and maps were collected through a NanoIR2 Anasys Instrument coupled with a multichip tunable quantum cascade laser (QCL; MIRcat-QT Daylight Solutions) used as an infrared source. The data were recorded in the tapping mode using commercially available silicon gold-coated tips (70 nm thick gold coating, 225 µm nominal length, and 28 µm nominal width) with a resonance frequency of 75 kHz and force constant of 3 N/m. The 5 % of the average QCL laser power (0.5 W) with a pulse length of 260 ns was applied. The presented range was 1700 cm^{-1} – 1350 cm^{-1} with 1 cm^{-1} spectral resolution. For increasing the signal-to-noise ratio (SNR) at each measured point, 3 spectra were averaged. The AFM-IR maps were obtained at a scan rate of 0.5 Hz with the tapping mode setpoint and drive strength set to 5.48 V and 30 %, respectively. The number points per line was 500. To monitor the sample conditions during the measurements, the AFM topography was collected after obtaining each series of the spectra. Moreover, the AFM-IR maps were recorded simultaneously with the topography. These approaches allowed us to confirm that upon experimental conditions no thermal damages of the samples occurred.

2.7. Data processing

The AFM-IR and AFM-SEIRA results together with the 2D intensity maps were processed with Analysis Studio version 3.14 software. The 3D intensity map was generated utilizing Mountainsmap 7.3 software (Digital Surf, France). To process and visualize the vibrational spectra

the Omnic 32 software was applied. The spectra were smoothed using the Savitzky-Golay filter (3rd-order polynomial and 5 data points). Additionally, multipoint baseline correction (5 points) was performed before normalization. Finally, the min–max normalization was used before the data interpretation.

3. Results and discussion

3.1. SERS investigations

Fig. 2 represents RS and SERS spectra of gefitinib immobilized on the AgNP and AuNP systems recorded using 532.0 nm (A, C) and 632.8 nm (B, D) laser lines, respectively. As it was mentioned in the Introduction part, the application of the two separate laser excitations was necessary for obtaining maximum signal reinforcement. This is associated with the different positions of the resonance band for AgNPs and AuNPs (please see Fig. S1, Supplementary material) what determines the amount of the surface enhancement [33,50]. The band assignments for the characteristic RS and SERS bands of gefitinib are provided in Table 1. The vibrational band interpretations are based on the conventional and surface-enhanced vibrational spectra of gefitinib [51], aniline [52], morpholine [53,54], fluoro derivatives of phenyl rings [55,56], and also quinazoline derivatives such as erlotinib [28,29,33,34,57,58]. Comparison between the SERS and the corresponding RS data shows unequivocally the dominance of the quinazoline moiety in the interaction of the investigated drug with both the AgNP and AuNP surfaces. This is manifested by the strong intensity SERS bands that appear at 1609 cm^{-1}, 1476 cm^{-1}, 1403 cm^{-1}, 1360 cm^{-1}, 1304 cm^{-1}, 828 cm^{-1}, 692 cm^{-1} and 1606 cm^{-1}, 1470 cm^{-1}, 1399 cm^{-1}, 1361 cm^{-1}, 1298 cm^{-1}, 829 cm^{-1}, 690 cm^{-1} for AgNPs and AuNPs, respectively. These bands are attributed to the $\nu(CC)_Q$, $\nu(CC)_Q/\nu(CN)_Q$, $\nu(C{=}N)_Q$, $\nu(CNC)_Q$, $\nu(CN)_Q/\nu(CC)_Q$, $\delta_{oop}(Q)$, $\nu_{i.p.}(Q)$, accordingly. Based on the surface selection rules established for the SERS technique, it is possible to elucidate how molecules orient on the metal surfaces. Observation of the particular SERS bands properties in relation to the conventional Raman spectral features, namely the relative intensities, the position of bands, and bandwidth changes indicate the spatial orientation of the functional groups which take part in the molecule/metal interaction. These differences originate from the interaction between the molecule and the metal and variations of the electric field components (tangential and normal) at the surface. Briefly, in the surface-enhanced spectra, the domination of the vibrations with polarizability derivative components normal to the roughened metal surface is distinguished [59,60]. Therefore, the bonds oriented perpendicular to the metal surface should be visible as the most intense bands in the surface-enhanced spectrum. The strong intensity of the characteristic quinazoline bands in the SERS spectrum indicates that gefitinib adsorbs of both types of metal surfaces through this moiety. This statement is also confirmed by the significant differences in the position ($\Delta\nu$) and bandwidth (Δ_{FWHM}; Full Width at High Maximum) of the particular bands, namely $\Delta\nu$ = 6 cm^{-1} and 7 cm^{-1}, Δ_{FWHM} = 11 cm^{-1} and 8 cm^{-1} of the $\nu(C{=}N)_Q$ modes, $\Delta\nu$ = 1 cm^{-1} and 8 cm^{-1}, Δ_{FWHM} = 3 cm^{-1} and 8 cm^{-1} of the $\nu(CNC)_Q$ modes, $\Delta\nu$ = 4 cm^{-1} and 6 cm^{-1}, Δ_{FWHM} = 5 cm^{-1} and 4 cm^{-1} of the $(CN)_Q/\nu(CC)_Q$ modes, $\Delta\nu$ = 3 cm^{-1}, and 1 cm^{-1}, Δ_{FWHM} = 2 cm^{-1} and 2 cm^{-1} of the $\nu_{i.p.}(Q)$ modes for the AgNPs and AuNPs, respectively. Due to the fact that, the most visible spectral properties change the bands from the C═N vibrations, this bond mainly interacts with the AgNPs and AuNPs. Additionally, in the SERS spectra, the signal enhancement of the bands attributed to the in-plane vibrations ($\delta_{i.p.}(Q)$) and weakening of the intensity of the bands due to the out-of-plane modes (($\delta_{i.p.}(Q)$) in comparison to the corresponding RS spectra is observed. Based on the discussed above surface selection rules, these spectral patterns prove the vertical orientation of the quinazoline on both metal surfaces. Such orientation enables the strong C═N/AgNPs and C═N/AuNPs connection discussed above. The adsorption geometry of the quinazoline moiety of gefitinib immobilized on the AgNPs and AuNPs does not

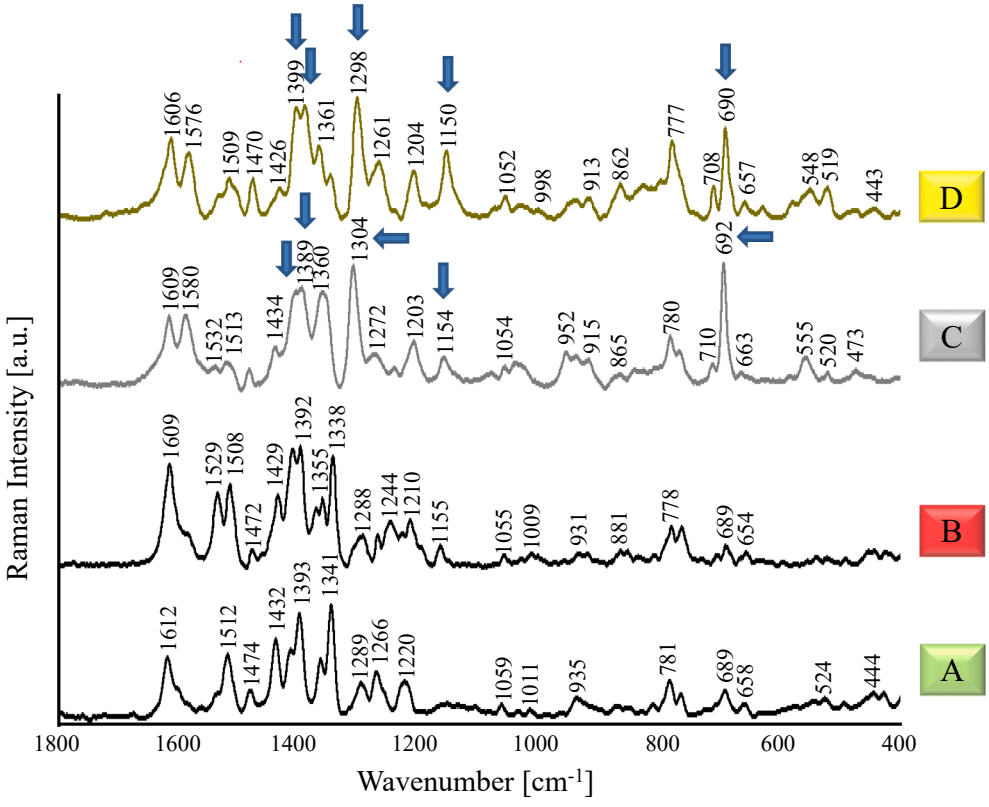

Fig. 2. Raman spectra of non-adsorbed gefitinib recorded using 532.0 nm (A) and 632.8 nm (B) laser lines together with the SERS spectra for this drug immobilized on the AgNP (C) and AuNP (D) surfaces in the spectral range of 1800– 400 cm^{-1}. The most important bands have been marked by arrows.

Table 1
The band assignments together with the wavenumbers (ν) and full width at half maximum (FWHM) for the significant RS bands of gefitinib non-adsorbed recorded using 532.0 nm and 632.8 nm laser lines, respectively, and for the SERS bands of this drug after its adsorption on the AgNP and AuNP surfaces.[28,29,33,34,51-58]

Band assignments[a]	Gefitinib				Gefitinib-AgNPs		Gefitinib-AuNPs	
	532.0 nm	FWHM [cm^{-1}]	632.8 nm	FWHM [cm^{-1}]	SERS	FWHM [cm^{-1}]	SERS	FWHM [cm^{-1}]
$\nu(CC)_{\phi}$, $\nu(CN)$, $\rho_b(NH)$	1612	17	1609	22	1609	16	1606	16
$\nu(CC)_Q$	1593	15						
$\nu(CC)_{Phe}$	1576	10	1580	25	1580	23	1576	21
ν(Phe), $\rho_b(NH)$, $\delta_{i.p.}(NH)$, $\nu(Q)$	1532	10	1529	16	1532	18	1527	17
ν(Phe), $\nu(CN)$, $\rho_w(OCH_3)$	1512	10	1508	15	1513	16	1509	15
$\rho_s(CH_2)_{OCH2}$, $\rho_s(CH_2)_{CH3}$					1502	10	1498	11
$\nu(CC)_Q$, $\nu(CN)_Q$	1474	25	1472	7	1476	10	1470	12
$\nu(CF)_{\phi}$	1432	16	1429	13	1434	20	1426	15
$\nu(C{=}N)_Q$, $\nu(CC)_Q$, $\rho_b(CH)_Q$, $\rho_b(NH)$, $\nu(Q)$, $\delta_{i.p.}(NH)$, $\delta_{i.p.}(CH)$	1409	14	1406	15	1403	25	1399	23
$\rho_w(CH_2)_{Mo}$, $\nu(C{=}N)_Q$	1393	15	1392	12	1389	20	1383	20
$\nu(CNC)_Q$	1361	13	1367	8	1360	19	1361	16
$\rho_b(NH)$			1355	8				
$\rho_w(CH_2)$	1341	12	1338	12	1347	16	1341	13
$\nu(CN)_Q$, $\nu(CC)_Q$, $\rho_t(CH_2)_{Mo}$	1300	12	1304	14	1304	17	1298	18
$\rho_t(CH)_{Mo}$, $\nu(CN)$	1289	17	1288	12				
$\nu(CN)/\nu(CN)_Q$	1266	15	1264	8	1272	30	1261	20
$\nu(CN)$, $\rho_b(NH)$	1252	11	1249	14				
$\nu(CO)_{OCH2}$			1241	16	1238	10	1237	6
$\rho_t(CH_2)_{non\text{-}synchronous;Mo}$, $\rho_b(CH)$, ν(Phe), $\rho_t(CH_2)$, $\nu(CH)$			1210	15	1203	23	1204	19
$\rho_t(CH_2)_{Mo}$, $\delta_{i.p.}(CH)$			1191	12				
$\nu_{as}(OCH_3)$, ν(quinazoline), $\nu(CN)_{Mo}$			1160	9	1154	15	1150	15
$\rho_r(CH_2)_{non\text{-}synchronous;Mo}$	1059	13	1055	10	1054	10	1052	13
$\nu_{i.p.}(CC)_{Mo}$	1034	4	1028	6	1036	18	1031	8
$\delta_{i.p.}$(Phe), $\nu_{i.p.}(CC)_{Mo}$	1011	12	1009	15	1019	8	1021	8
$\delta(\phi)_{Phe}$, δ(Phe)							998	11
$\nu_{i.p.}(CN)_{Mo}$, $\nu_{i.p.}(CO)_{Mo}$					915	18	913	14
$\nu_{i.p.}(CN)_{Mo}$, $\nu_{i.p.}(CO)_{Mo}$	868	9			865	13	862	18
$\nu(CC)_{Mo}$, $\nu(CO)_{Mo}$	849	14			843	15		
$\delta_{oop}(Q)$, $_{(in\text{-}plane\ ring\ breathing)Mo}$					828	10	829	18
ν(Phe), $\nu(Q)$	781	14	778	10	780	14	777	16
$\rho_{boop}(CH)_{Phe}$	762	11	760	17	763	16	764	18
$\nu_{i.p.(}CNC)_{Mo}$	706	9			710	10	708	7
$\nu_{i.p.}(Q)$	689	17	689	13	692	19	690	15
$\delta_{oop}(NH)$	658	13	654	11	663	9	657	15
$\rho_{boop}(CH_2)_{Phe}$	524	19	519	15	520	15	519	20
$\rho_b(CNC)_{Mo}$, $\rho_b(COC)_{Mo}$, $\delta_{oop}(NH)$			453	17				
$\rho_b(CNC)_{Mo}$, $\rho_b(COC)_{Mo}$	444	15	441	9			443	12

[a]Abbreviations: ν, stretching; ρ_b, bending; ρ_w, wagging; ρ_s, scissoring; ρ_r, rocking; δ, deformation; as, antisymmetric; oop, out-of-plane; i.p., in-plane; Phe, phenyl ring; Q, quinazoline group; Mo, morpholine

correspond with this observed for erlotinib (another quinazoline derivative; drug applied in the targeted therapy for non-small cell lung cancer) [28,33]. Briefly, erlotinib adsorbs on the AgNPs mainly through the phenylacetylene ring, the amino and the methoxy groups. While the quinazoline moiety indicates rather weak interaction with these NPs. For the erlotinib/AuNPs connections, the phenylacetylene ring and quinazoline moiety play the main role. Although for both gefitinib and erlotinib quinazoline moiety interacts with these metal NPs through the N═C bond, this interaction is definitely stronger for the former than for the latter drug.

The spectral pattern illustrated in the SERS spectra of gefitinib immobilized on the AgNPs and AuNPs (see Fig. 2, respectively), indicates the crucial participation of another functional group in the drug/metal NPs interactions. The bands occurring at 1389 cm^{-1}, 1203 cm^{-1}, 1054 cm^{-1}, 1036 cm^{-1}, 1019 cm^{-1}, 915 cm^{-1}, 865 cm^{-1}, 710 cm^{-1} and 1383 cm^{-1}, 1204 cm^{-1}, 1052 cm^{-1}, 1031 cm^{-1}, 1021 cm^{-1}, 913 cm^{-1}, 862 cm^{-1}, 708 cm^{-1} in the SERS spectra of AgNPs and AuNPs, respectively, are characteristic for the morpholine vibrations. More specifically, they result from the $\rho_w(CH_2)$, $\rho_t(CH_2)_{non\text{-}synchronous}$, $\rho_r(CH_2)_{non\text{-}synchronous}$, $\nu_{i.p.}(CC)$, $\nu_{i.p.}(CC)$, $\nu_{i.p.}(CN)/(CO)$, $\nu_{i.p.}(CN)/(CO)$, $\nu_{i.p.}(CNC)$ motions, accordingly (see Table 1). The literature data reports that the morpholine adsorption on the AuNPs is associated with its concentration [54]. The high concentration of morpholine favors vertical orientation on the metal surface and strong interaction through the N atom. Together with the dilution, the horizontal adsorption is suggested. In the case of gefitinib, the N atom of the morpholine moiety is substituted by the methylene bridge which may prevent its strong interaction with the metal NPs (see Fig. 1 for molecular structure). Thus, the morpholine/AgNPs and morpholine/AuNPs connections through the O atom or CH_2 groups are expected. Indeed, the strong enhancement of the mentioned above bands at 1389 cm^{-1} and 1383 cm^{-1}, in the SERS spectra on AgNPs and AuNPs, respectively, are attributed to the wagging vibrations of the CH_2 group linked to the O atom in the morpholine molecular structure. Moreover, the intensification of the SERS bands at 1304 cm^{-1} and 1298 cm^{-1} assigned to the stretching vibrations of the C—N and C—C of quinazoline may suggest the participation of the morpholine moiety vibrations to these bands as well. The twisting motions of the CH_2 group situated to the O atom can contribute to the observed strong intensity of the above-mentioned bands. The reinforcement of these bands is quite spectacular since they indicate very weak intensity in the corresponding RS spectra (see Fig. 2). The discussed spectral pattern, which shows the enhancement of the in-plane bands of morpholine, implies its vertical orientation on the applied metal NPs. However, the stronger interaction between this functional group and the AuNPs than for the AgNPs is assumed. This statement is supported by the observed significant shift and broadening of the characteristic morpholine SERS bands of gefitinib adsorbed on the AuNPs in comparison with the corresponding RS spectral features (i.e. $\Delta\nu = 9\ cm^{-1}$, $\Delta_{FWHM} = 8\ cm^{-1}$ for the band at 1383 cm^{-1}, $\Delta\nu = 6\ cm^{-1}$, $\Delta_{FWHM} = 4\ cm^{-1}$ for the band at 1298 cm^{-1}). For gefitinib/AgNPs these changes in relation to the corresponding RS

spectral features seems not to be so spectacular, namely $\Delta\nu = 9$ cm^{-1}, $\Delta_{FWHM} = 5$ cm^{-1} and $\Delta\nu = 4$ cm^{-1}, $\Delta_{FWHM} = 5$ cm^{-1}, respectively (please see Table 1). Additionally, the medium intensity band at 828 cm^{-1} appearing in the considered gefitinib/AuNPs SERS spectrum may be assigned to the stretching vibrations of the CO bond [$\nu_{i.p.}$(CO)] what indicates the participation of the O atom in the discussed interaction. It should be noted that this band is only negligible enhanced in the gefitinib/AgNPs SERS spectrum (please see Fig. 2).

The participation of the methoxy moiety of gefitinib in the AgNPs and AuNPs interactions is also noteworthy. The bands appearing at 1513 cm^{-1} and 1509 cm^{-1}, 1154 cm^{-1} and 1150 cm^{-1} in the SERS spectra, respectively, represent $\rho_w(OCH_3)$ and $\nu_{as}(OCH_3)$ motions. The strong enhancement, broadening, and position shift are noticed for the SERS bands resulting from the latter vibrations, namely these which represent asymmetric stretching modes of the methoxy group [$\nu_{as}(OCH_3)$; $\Delta\nu = 10$ cm^{-1} and $\Delta_{FWHM} = 6$ cm^{-1}, please see Table 1]. This spectral pattern is well observable for the gefitinib/AgNPs and gefitinib/AuNPs spectra. At the same time, the intensity of the bands at 1513 cm^{-1} and 1509 cm^{-1} decreases in the SERS spectra of gefitinib immobilized on the AgNPs and AuNPs, accordingly, in comparison with the corresponding RS bands. However, taking into account the nature of the considered vibrations, it should be noted that the perpendicular orientation of the methoxy moiety on the AgNP and AuNP surfaces could be responsible for such spectral phenomena.

In the discussed SERS spectra also bands involved in the vibrations attributed to the amino group and propoxy moiety occur. These bands are visible at 1532 cm^{-1}, 1347 cm^{-1}, 1238 cm^{-1}, and 1527 cm^{-1}, 1341 cm^{-1}, 1237 cm^{-1} for the gefitinib/AgNPs and gefitinib/AuNPs conjugates, respectively. Assignments of these spectral features are as follows ρ_b(NH), $\rho_w(CH_2)$, and $\nu(CO)_{OCH2}$, accordingly. The detected weak intensity of them in comparison with the corresponding RS bands suggests that the above-mentioned moieties do not participate strongly in the drug/metal NPs interaction. However, both are situated at a certain distance from the surfaces. Similar conclusions can be drawn after the analysis of the characteristic SERS band of the 3-chloro-4-fluorophenyl. Its spectral features appear at 1434 cm^{-1} [ν(CF)], 763 cm^{-1} [ρ_{boop}(CH)], 520 cm^{-1} [ρ_{boop}(CH)], and 1426 cm^{-1} [ν(CF)], 764 cm^{-1} [ρ_{boop}(CH)], 519 cm^{-1} [ρ_{boop}(CH)] in the SERS spectra of AgNPs and AuNPs, respectively. The relatively weak enhancement of the listed bands in comparison to these observed in the corresponding RS spectra also implied that the 3-chloro-4-fluorophenyl rather does not play a significant role in the regarded drug/metal NPs interaction. Nevertheless, the noticed out-of-plane bands of this aromatic moiety, which are the slightly higher intensity for gefitinib/AuNPs than for the gefitinib/AgNPs, indicates tilted orientation. This spectral pattern can be explained in two ways. Firstly, the angle between the 3-chloro-4-fluorophenyl and the metal surface is lower for the AuNPs than for the AgNPs. Secondly, the distance at which the aromatic ring is situated from the metal is longer for the AgNPs than for the AuNPs. However, the stronger intensity of the bands due to the stretching vibrations of the CF bond visible in the SERS spectrum of gefitinib/AgNPs than for the gefitinib/AuNPs supports the first discussed explanation. Namely, the higher angle between the aromatic moiety and the AgNPs provides closer contact with the CF bond and the metal NPs than it could be possible in the case of a more horizontal orientation.

3.2. Tapping AFM-IR investigations

The drawn adsorption geometry of gefitinib on the AgNPs and AuNPs using the SERS technique was compared with the information obtained

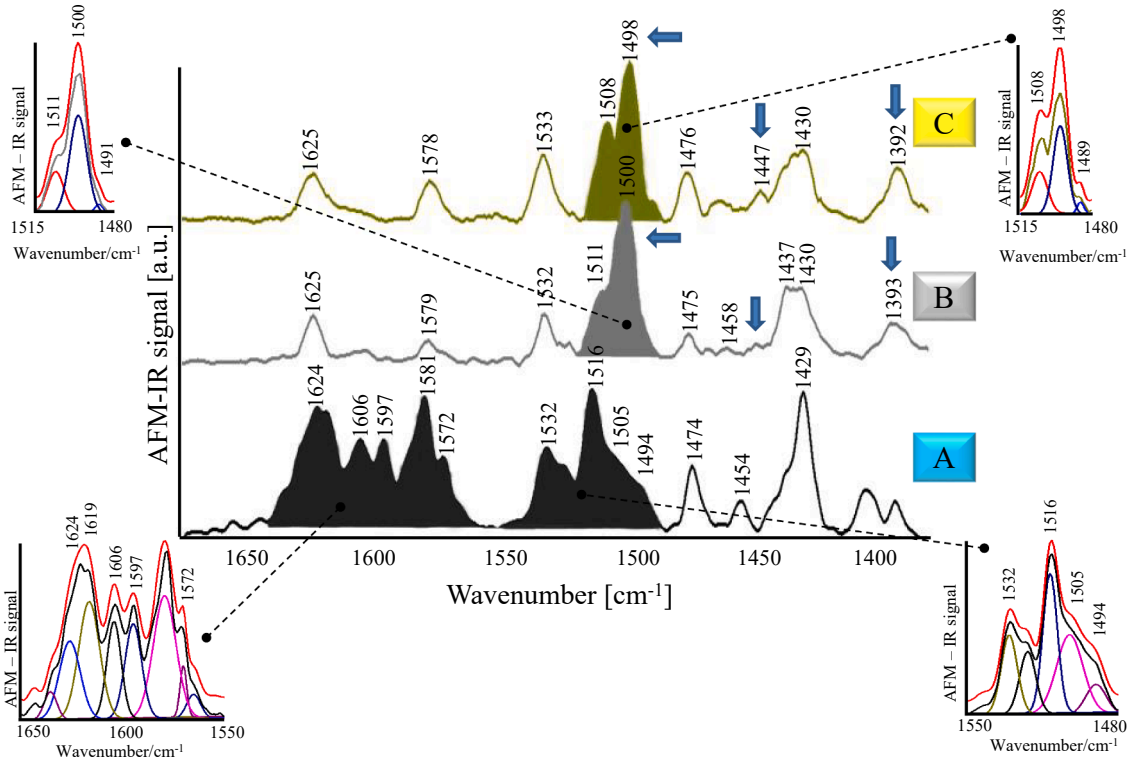

Fig. 3. AFM-IR spectrum of non-adsorbed gefitinib (A) together with the AFM-SEIRA spectra for this drug immobilized on the AgNP (B) and AuNP (C) monolayers in the spectral range of 1375– 1700 cm^{-1} together with the performed curve fitting; red solid lines illustrate the composite result spectra, while black, grey, and yellowish-brown solid lines represent the appropriate original spectra.

employing AFM-IR. Fig. 3 illustrates the AFM-IR data for non-adsorbed gefitinib and after its adsorption on the AgNP and AuNP mono-layers, respectively. Similar to the SERS spectra, the most intense bands in the surface-enhanced AFM-IR (AFM-SEIRA) results belong to the quinazoline moiety (please see Fig. 3). These spectral features, assigned to the $\nu(CC)_Q/\nu(C{=}N)_Q$ vibrations, appear at 1500 cm^{-1} and 1498 cm^{-1} for AgNP and AuNP mono-layers, respectively (please see Table 2 for the band assignments). The SEIRA surface selection rules clearly show that the bands of the vibrations, which generate the dipole changes oriented perpendicular to the metal surface reveal the most enhanced intensity [30,32]. In the light of these considerations, the domination in the AFM-SEIRA spectra bands due to the quinazoline, indicates that this moiety adopts vertical orientation on the nanoparticle surfaces. Moreover, the observed broadening and shift position of the aforementioned bands, namely Δ_{FWHM}= ~3 cm^{-1} and $\Delta\nu$=~5 cm^{-1}, respectively (please see Table 2), allow for concluding that the gefitinib/AgNP mono-layer and the gefitinib/AuNP mono-layer connections through the C=N bond of quinazoline are rather strong.

Without a doubt, also the morpholine moiety plays a crucial role in the gefitinib/AgNP and gefitinib/AuNP interaction. In the AFM-SEIRA spectra, it is reflected especially in the visible enhanced bands appearing at 1449 cm^{-1} [$\delta(CH_2)_{Mo}$], 1393 cm^{-1} [$\rho_w(CH_2)_{Mo}$] and 1447 cm^{-1} [$\delta(CH_2)_{Mo}$], 1392 cm^{-1} [$\rho_w(CH_2)_{Mo}$] for AgNP and AuNP mono-layers, respectively, in comparison with the corresponding AFM-IR spectrum for the non-adsorbed drug. Like it was distinguished based on the SERS spectra, also the spectral pattern observable in the AFM-SEIRA data indicates a closer connection of the morpholine with the AuNPs than it is detected for the AgNPs. This finding is based on the noticed stronger enhancement of the considered bands in the AFM-SEIRA spectrum for AuNP mono-layer than it occurs for the AgNP mono-layer (see Fig. 3).

The AFM-SEIRA spectra also illustrate the medium and weak intensity bands attributed to the 3-chloro-4-fluorophenyl, amino moiety, and propoxy group. These bands are observed at 1579 cm^{-1} [$\rho_b(CH)_{Phe}$], 1532 cm^{-1} [$\rho_b(NH)$], 1475 cm^{-1} [$\rho_w(CH_2)_{CH3}$], 1437 cm^{-1} [$\nu(CH)_{Phe}$], 1430 cm^{-1} [$\rho_w(CH_2)_{CH3}/\rho_w(CH_2)_{OCH2}/\rho_w(CH_2)$] and 1578 cm^{-1} [$\rho_b(CH)_{Phe}$], 1533 cm^{-1} [$\rho_b(NH)$], 1476 cm^{-1} [$\rho_w(CH_2)_{CH3}$], 1437 cm^{-1} [$\nu(CH)_{Phe}$], 1430 cm^{-1} [$\rho_w(CH_2)_{CH3}/\rho_w(CH_2)_{OCH2}/\rho_w(CH_2)$] for the AgNP and AuNP mono-layers, respectively. Non-observable enhancement of the aforementioned bands together with no changes in their positions and widths in comparison with the corresponding AFM-IR spectrum for non-adsorbed drug (please see Table 2) confirms that the considered functional groups do not take a crucial role in the gefitinib/metal NPs interactions. The suggested orientation of gefitinib on the AgNP and AuNP mono-layers, respectively, are provided in Fig. 4.

The application of the two surface-enhanced techniques namely SERS and AFM-SEIRA allows for performing deep investigations of how gefitinib connects with two different types of metal NPs. Moreover, the obtained data from two approaches which are based on two different physical phenomena: the Raman scattering (SERS) and the thermal expansion (AFM-SEIRA) effects, allow to reach the same conclusions about the drug/metal NPs interaction. This also gives a piece of strong evidence that the AFM-IR is sensitive to the enhancement phenomenon appearing on the metal surface (thus the introduction of the term AFM-SEIRA is appropriate), and can be successfully used for the characterization of molecules' adsorption on the metal surfaces with the ultra-high resolution reached even 15 nm by applying the well-known surface selection rules [30].

Table 2
The band assignments together with the wavenumbers (ν) and full width at half maximum (FWHM) for the significant AFM-IR bands of gefitinib non-adsorbed and the AFM-SEIRA bands of this drug after its adsorption on the AgNP and AuNP surfaces.[28,29,33,34,51-58].

Band assignments[a]	Gefitinib		Gefitinib-AgNPs		Gefitinib-AuNPs	
	AFM-IR	FWHM [cm^{-1}]	AFM-SEIRA	FWHM [cm^{-1}]	AFM-SEIRA	FWHM [cm^{-1}]
$\nu(CC)_{Phe}$, $\rho_b(NH)$, $\nu(CN)_Q$	1624	12	1625	7	1625	10
$\nu(CC)_Q$	1619	12	1612	11	1614	11
$\nu(CC)_{Phe}$, $\rho_b(NH)$, $\nu(C{=}N)_Q$, $\nu(CC)_Q$	1606	8	1605	9		
$\nu(CC)_Q$	1597	9				
$\rho_b(NH)$, $\nu(NC)_{Q\text{-}NH}$, $\nu(C{=}N)_Q$, $\nu(CC)_{CPheC}$, $\rho_b(CH)_{Phe}$, $\nu(CC)_Q$	1581	13	1579	8	1578	8
$\nu(CC)_{Phe}$	1572	7				
$\rho_b(NH)$	1532	8	1532	6	1533	8
$\rho_w(OCH_3)$	1514	7	1511	8	1508	8
$\nu(CC)_Q$, $\nu(C{=}N)_Q$, $\rho_b(CH)_Q$	1505	7	1500	10	1498	10
$\rho_b(CH)_{Phe}$, δ(Phe)	1494	10	1491	4	1489	3
$\rho_w(CH_2)_{CH3}$	1474	6	1475	5	1476	6
$\rho_b(CH)_Q$, $\nu(CN)_Q$, $\nu(CC)_Q$	1460	7	1460	9	1460	10
$\delta(CH_2)_{Mo}$			1449	9	1447	10
$\nu(CH)_{Phe}$	1435	11	1437	6	1437	7
$\rho_w(CH_2)_{CH3}$, $\rho_w(CH_2)_{OCH2}$, $\rho_w(CH_2)$	1429	8	1430	8	1430	8
$\rho_w(CH_2)_{CH3}$, $\rho_w(CH_2)_{OCH2}$, $\rho_w(CH_2)$, $\rho_b(NH)$, δ(Q)			1422	9	1421	10
$\rho_b(NH)$	1404	10				
$\rho_w(CH_2)_{Mo}$	1393	6	1393	10	1392	11

[a]Abbreviations: ν, stretching; ρ_b, bending; ρ_w, wagging; ρ_s, scissoring; δ, deformation; Phe, phenyl ring; Q, quinazoline group; Mo, morpholine

3.3. Spectral signal enhancement comparison

The complementary of the surface enhancement phenomenon appearing in both considered techniques, namely SERS and AFM-SEIRA is also observed in the signal amplification which is received on different types of metals. It is commonly known that AgNPs ensure higher spectral signal reinforcement in comparison with the AuNPs of the same size and shape. This is strongly connected to their optical properties which allow maintaining strong plasmon resonance at the specific resonance wavelength. Briefly, the amount of the electromagnetic field created on the metal surface depends on the incoming electromagnetic waves and the field produced by the surface metal plasmons [40]. This combined electromagnetic field for the spherical NPs is related to the size of NPs, their electric permittivity, and the environment [40,61]. When the size of NPs, the environment, and the energy of irradiating waves are fixed, so the used NPs possess the same radius, the measurements are performed in the same conditions with the same wavelength, the obtained electromagnetic field enhancement is determined by the electric metal properties. Rycenga and co-workers [62] presented deep considerations of what affects the ability of metal nanostructure to maintain the surface plasmon resonance effect. The main factor of effective interaction between the surface electrons and the light is the dielectric function of the metal, which contains its real and imaginary parts and are different for various excitation wavelengths. Although the negative value of the real part of the dielectric function provides the strong surface plasmon resonance, at the same time the imaginary part needs to be close to zero [40,62,63]. Comparing these parameters for the AgNPs and AuNPs, respectively, it should be noted that the AgNPs indicate the highest real part and the lowest value of the imaginary part of the dielectric function in the visible and near-infrared region [62]. Thus, for these NPs the conditions necessary for strong resonance are fully met. In other words, the application of AgNPs allows for obtaining larger spectral signal enhancement than it is provided by the AuNPs. This effect occurs in the SERS as well as in the SEIRA occurrences [62,64]. Fig. 5 shows the comparison of the corresponding SERS and AFM-SEIRA spectra for the drug/AgNP and the drug/AuNP systems. Presented data confirm that the AgNPs increase spectral signal a few times stronger than the AuNPs.

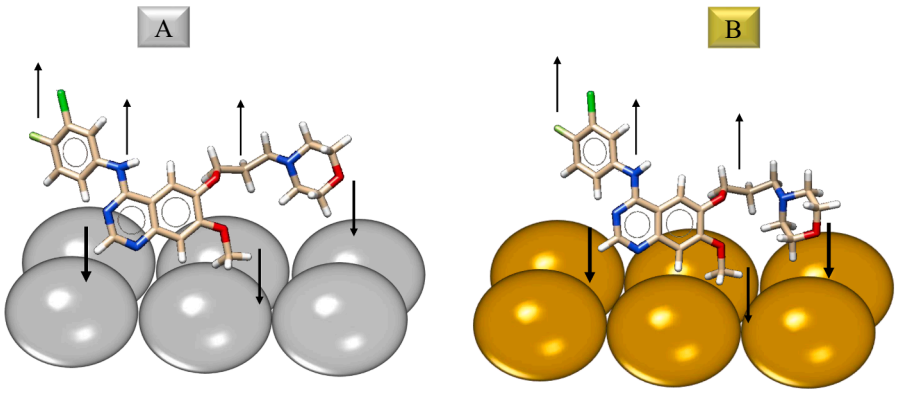

Fig. 4. The suggested gefitinib adsorption geometry on the AgNP (A) and AuNP (B) mono-layers. Direction of the interactions are indicated by arrows. Thicker arrows equate to a stronger effect.

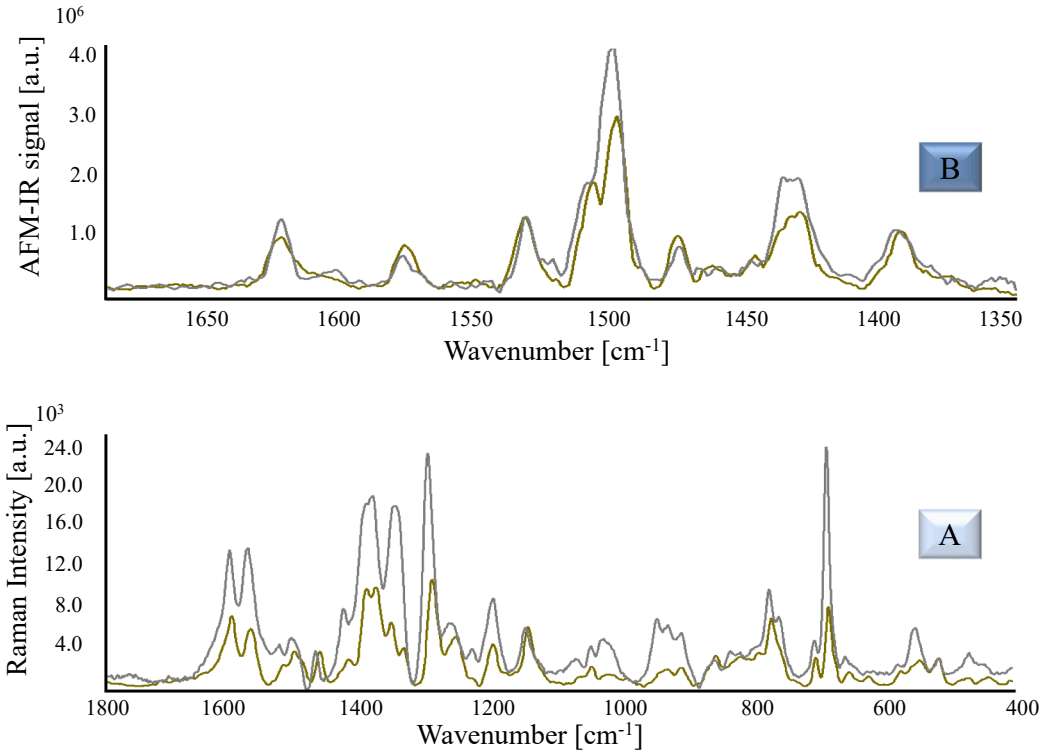

Fig. 5. SERS (A) and AFM-SEIRA (B) spectra of gefitinib/AgNPs (grey lines) and gefitinib/AuNPs (yellowish-brown lines) in the spectral ranges 1800 – 400 cm^{-1} and 1700 – 1350 cm^{-1}, respectively.

These spectral patterns confirm the complementarity between the phenomena of the well-known SERS and SEIRA techniques and the quite new AFM-SEIRA approach.

The AFM-IR technique ensures also unique information about the spectral signal distribution on the regarded metal mono-layers. Fig. 6 represents the topographies of the AgNP and AuNP mono-layers, respectively, with the immobilized drug, together with the AFM-SEIRA maps. These maps illustrate the intensity distribution of the most enhanced bands in the AFM-SEIRA spectra namely these attributed to the $\nu(CC)_Q/\nu(C{=}N)_Q$ vibrations. One can be noticed that the strongest spectral signal occurs on the particular nanoparticle surfaces instead of the space between them, as was expected. This phenomenon is even better observed in the 2D and 3D 200 nm × 200 nm AFM-SEIRA maps of gefitinib adsorbed on the AgNP mono-layer (please see Fig. 7). Additionally, the comparison between the profile analysis of the AFM-SEIRA and AFM height signals also confirms clearly that the strong enhancement of the spectral signal appears on the top of particular NPs (Fig. 7D). As it was mentioned in the Introduction past, the previously published AFM-SEIRA data for erlotinib immobilized on the AgNP mono-layer [29] the spectral signal distribution observed in the AFM-SEIRA maps corresponds very well with the “hot spot” theory, which manifests that the strongest signal enhancement should appear between the spherical NPs. However, the image of the signal distribution presented for gefitinib/AgNP mono-layer sheds new light on the AFM-SEIRA map interpretation for molecules adsorbed on the metal surfaces. Based on the fact that in these two considered systems namely erlotinib/AgNP mono-layer and gefitinib/AgNP mono-layer the same type of metal NPs were used, one may be excluded that the NPs themselves affect the spectral signal distribution. On the other hand, the gold-coated tip applied in the NanoIR2 system with the laser illumination from the top may also have a crucial influence on the occurred signal distribution. Lu and co-workers [65] discussed the possible

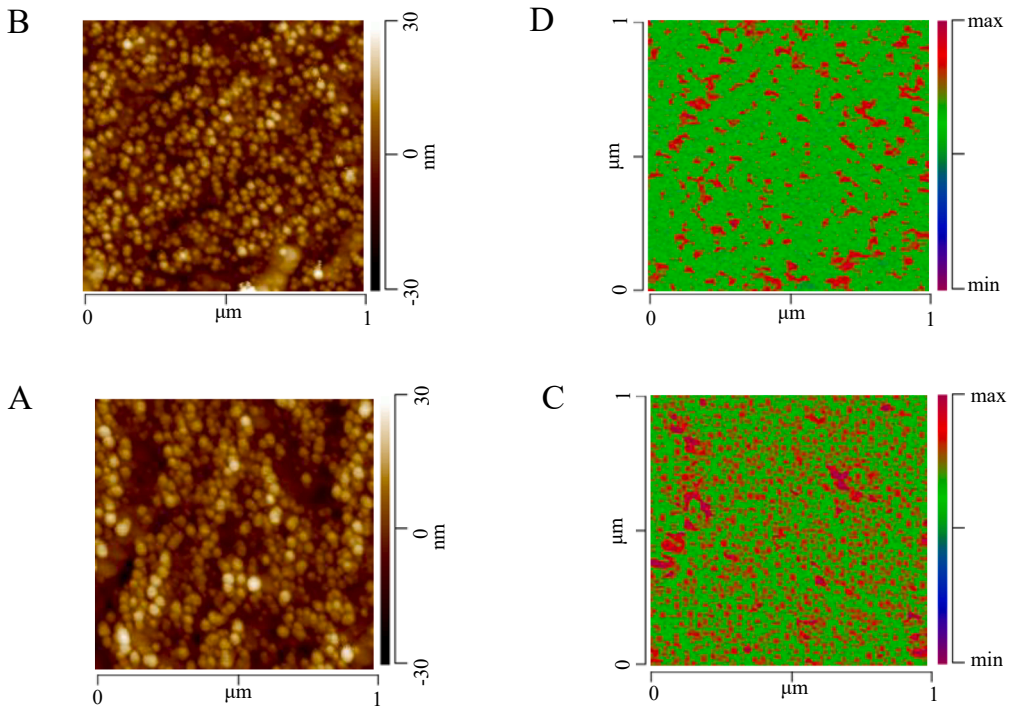

Fig. 6. The AFM topographies 1 µm × 1 µm of the AgNP (A) and AuNP (B) mono-layers with the adsorbed gefitinib together with the AFM-SEIRA intensity maps of the bands at ~ 1500 cm^{-1}(C) and (D), respectively).

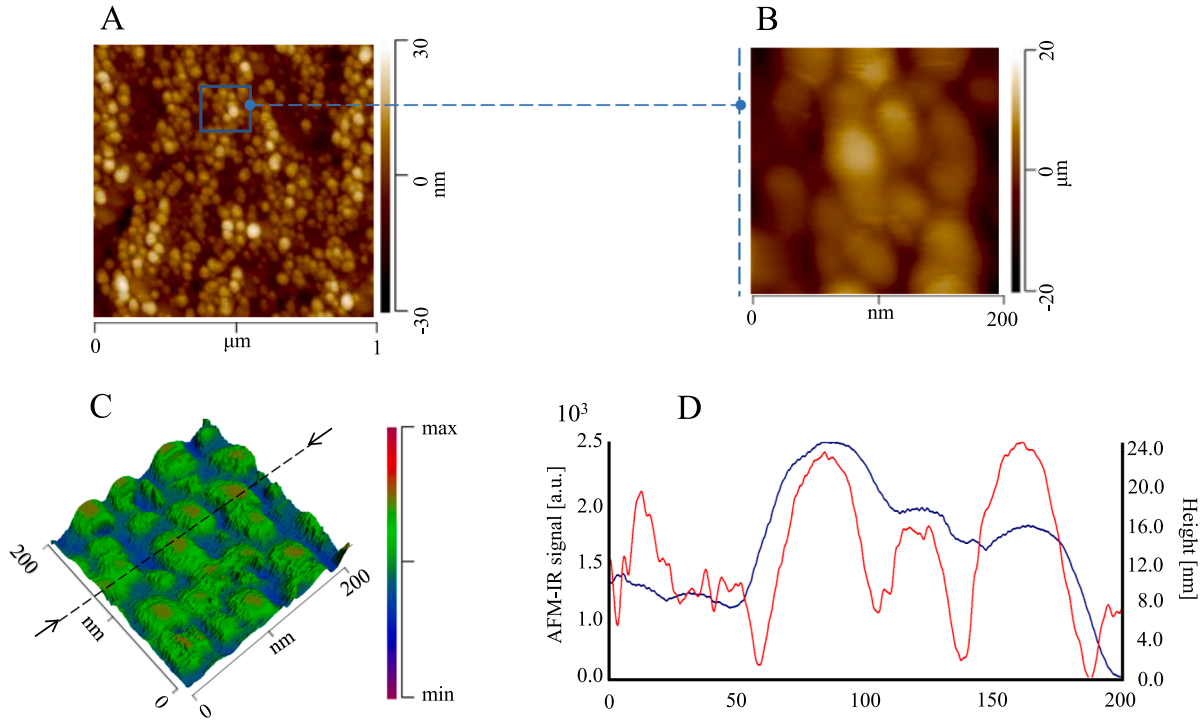

Fig. 7. The AFM topographies 1 µm × 1 µm (A) and 200 nm × 200 nm (B) of the gefitinib/AgNP mono-layer together with the 3D AFM–SEIRA intensity map of the band at 1500 cm^{-1}(C) and AFM-IR signal (red line) compared with height profile (blue line) at the position marked in (C) with a black dotted line and arrows (D).

electromagnetic field enhancement appearance when the gold-coated tip and the flat gold metal surface are used. In the gap forming between the two metals (tip and the surface) the additional optical field effectively increases the sensitivity and the spatial resolution. Such resolution now depends on the "hot spot" size occurring in this nanogap. Although this statement is still not clear, especially for the roughened metal surfaces (such as metal nanoparticle mono-layers), it should be noted that a comparable signal distribution of gefitinib on the AgNP mono-layer was obtained with a different tip (data not shown). Nevertheless, the AFM-SEIRA signal enhancement obtained using two

different types of metal NPs described above are in good agreement with the surface plasmon resonance theory, and with what is already known for the SERS and SEIRA signal reinforcement. Therefore, the electromagnetic enhancement phenomenon should be reflected in the AFM-SEIRA intensity maps. These considerations may lead to the conclusion that the spectral signal distribution of the molecule immobilized on the metal mono-layer drawn by the AFM-SEIRA maps is connected to the nature of the molecule/metal interaction. On the one hand, if the molecules present a strong interaction with metal NPs, it will induce their aggregation [66,67], and reduce the distance in between. As a consequence, the strongest enhancement should occur between the nanostructures. On the other hand, if the molecules interact moderately with the metal NPs, their aggregation is weak and the distance between the gold-coated tip and the surface of the metal nanoparticle is shorter than between the neighboring metal NPs. As a consequence, the strongest enhancement will be observed between the gold-coated tip and the surface of some specific NPs. Thus, the distribution of the enhanced signal (in between or on top of the NPs) will guide us to decipher which phenomenon occurs. These statements seem reasonable based on the data collected for erlotinib and gefitinib-metal NPs sample. Briefly, the significant spectral signal changes (band broadening and shift position) observed for characteristic bands of particular functional groups in the previously published RS spectra of erlotinib in comparison with the corresponding SERS results after its adsorption on the AgNPs and AuNPs proves the very strong connection between this drug and the metal NPs [28,33]. Furthermore, both charge transfer and bond creation between the molecule and the metal result in dramatic spectral pattern changes in the surface-enhanced spectra as well as additional spectral signal reinforcements. Such extraordinary signal amplification is additionally determined by nanoparticle aggregation [68–70] (a key factor of "hot spot" formation), clearly visible in the AFM topographies of erlotinib/AgNP and erlotinib/AuNP mono-layers, respectively [29]. For gefitinib, the SERS spectra received after its adsorption on the AgNPs and AuNPs do not illustrate so strong changes in comparison with the RS spectra for the non-adsorbed drug (please see Fig. 2). Moreover, the AFM topographies presented in Fig. 6 do not reveal such strong aggregation of the NPs as it was noticed in the case of erlotinib [29].

4. Conclusions

In this study, the detailed characterization of how gefitinib interacts with AgNPs and AuNPs, considered as potential drug nanocarriers, using SERS and AFM-SEIRA techniques was performed. The obtained results indicate the connection between the drug and the metal NPs mainly through the quinazoline and morpholine moieties. Additionally, this connection seems to be stronger for gefitinib/AuNP than for the gefitinib/AgNP conjugates. The verification of the AFM-SEIRA results by the simultaneous SERS analysis proves the usefulness of this quite new approach for the interpretation of molecule/metal interaction with ultra-high spatial resolution of ~ 15 nm, which corresponds to the size of the particular nanoparticle. However, to date, the evidence confirming the complementary information obtained using SERS and AFM-SEIRA and the validity of using the latter technique was rather poor. The performed considerations supported by the previously published data [29] proved unequivocally that the surface phenomenon observed in the well-known techniques such as SERS and SEIRA also occurs in the AFM-SEIRA. Moreover, the surface selection rules applied for the interpretation of the adsorption geometry of molecules on the metal surfaces allow for the elucidation of the spectral changes observed in the AFM-SEIRA spectra in comparison with the corresponding AFM-IR results for the molecules non-adsorbed on metal NPs. These changes are manifested in the relative intensity, position, and width of bands from the particular functional groups involve in the interaction with the metal NPs.The complementarity between the AFM-SEIRA effect and conventional SEIRA and SERS was also indicated based on the analyzed signal enhancement depending on the type of the applied metal NPs. The optical properties of the metals determining the maintenance of the surface plasmon resonance which affect the obtained signal reinforcement in the conventional surface-enhanced vibrational spectra also influence the signal enhancement in the AFM-SEIRA results. Typically, the silver NPs ensure a stronger enhancement phenomenon than gold NPs for SEIRA and SERS. The same statement has been proved for AFM-SEIRA effect. Finally, taking into account the whole performed considerations one may be concluded that the AFM-SEIRA maps bring out the enhancement distribution which is directly linked to the nature of molecule/metal interaction. Indeed, a strong interaction of the studied molecules with the NPs promotes their aggregation resulting in the appearance of the strong AFM-SEIRA signal between adjacent NPs. A strong AFM-SEIRA signal between adjacent NPs could also be observed if the NPs aggregation trapping more molecules in the space between them than on their top. Thus, the postulate that the AFM-SEIRA map illustrates the distribution of the molecule on the metal mono-layer surface may still be correct. In the case of a weak NPs aggregation, the enhanced electromagnetic field generated between the gold-coated AFM tip and the metal NPs may prevail.

CRediT authorship contribution statement

Natalia Piergies: Conceptualization, Methodology, Validation, Formal analysis, Writing – original draft, Writing – review & editing, Visualization, Project administration, Funding acquisition. **Jérémie Mathurin:** Resources, Validation, Writing – original draft. **Alexandre Dazzi:** Resources, Validation, Writing – original draft, Funding acquisition. **Ariane Deniset-Besseau:** Resources, Validation, Writing – original draft. **Magdalena Oćwieja:** Methodology, Validation, Formal analysis, Writing – original draft, Writing – review & editing, Visualization. **Czesława Paluszkiewicz:** Supervision, Validation, Writing - original draft. **Wojciech M. Kwiatek:** Supervision, Funding acquisition.

Declaration of Competing Interest

The authors declare that they have no known competing financial interests or personal relationships that could have appeared to influence the work reported in this paper.

Data availability

Data will be made available on request.

Acknowledgments

This work was supported by the National Science Centre Poland (No. 2016/21/D/ST4/02178 to N. P.). N. P. gratefully acknowledges the financial support of the French Government and the French Embassy in Poland. These researches were also supported by the Paris Ile-de-France Region–DIM Materiaux anciens et patrimoniaux. The measurements were partly performed using the equipment purchased in the frame of the project co-funded by the Małopolska Regional Operational Program Measure 5.1 Krakow Metropolitan Areas an important hub of the European Research Area for 2007 – 2013, project no. MRPO.05.01.00-12-013/15e. The Authors are grateful to Dr. Dorota Duraczyńska for her invaluable help in the characterization of nanoparticles and nanoparticle monolayers with the use of TEM and SEM.

Appendix A. Supplementary material

Supplementary data to this article can be found online at https://doi.org/10.1016/j.apsusc.2022.155217.

References

[1] A. Dazzi, C.B. Prater, AFM-IR: Technology and Applications in Nanoscale Infrared Spectroscopy and Chemical Imaging, Chem. Rev. 117 (7) (2017) 5146–5173.

[2] C. Marcott, M. Lo, K. Kjoller, C. Prater, D.P. Gerrard, Applications of AFM-IR—Diverse Chemical Composition Analyses at Nanoscale Spatial Resolution, Micros. Today 20 (6) (Nov. 2012) 16–21, https://doi.org/10.1017/s1551929512000776.

[3] P. Nguyen-Tri, P. Ghassemi, P. Carriere, S. Nanda, A. A. Assadi, D. D. Nguyen, "Recent applications of advanced atomic force microscopy in polymer science: A review," *Polymers*, vol. 12, no. 5. MDPI AG, May 01, 2020. doi: 10.3390/POLYM12051142.

[4] J. Waeytens, V. Van Hemelryck, A. Deniset-Besseau, J.M. Ruysschaert, A. Dazzi, V. Raussens, Characterization by nano-infrared spectroscopy of individual aggregated species of amyloid proteins, Molecules 25 (12) (Jun. 2020), https://doi.org/10.3390/molecules25122899.

[5] C. Paluszkiewicz, N. Piergies, P. Chaniecki, M. Rękas, J. Miszczyk, W.M. Kwiatek, Differentiation of protein secondary structure in clear and opaque human lenses: AFM – IR studies, J. Pharm. Biomed. Anal. 139 (May 2017) 125–132, https://doi.org/10.1016/j.jpba.2017.03.001.

[6] C. Paluszkiewicz, N. Piergies, M.C. Guidi, E. Pięta, W. Ścierski, M. Misiołek, B. Drozdzowska, P. Ziora, G. Lisowska, W.M. Kwiatek, Nanoscale infrared probing of amyloid formation within the pleomorphic adenoma tissue, Biochim. Biophys. Acta - Gen. Subj. 1864 (10) (2020) 129677.

[7] M. Roman, T.P. Wrobel, C. Paluszkiewicz, W.M. Kwiatek, Comparison between high definition FT-IR, Raman and AFM-IR for subcellular chemical imaging of cholesteryl esters in prostate cancer cells, J. Biophotonics 13 (5) (2020) 1–14, https://doi.org/10.1002/jbio.201960094.

[8] L. Huang, X. Zhang, J. Shao, Z. Zhou, Y. Chen, X. Hu, Nanoscale chemical and mechanical heterogeneity of human dentin characterized by AFM-IR and bimodal AFM, J. Adv. Res. 22 (Mar. 2020) 163–171, https://doi.org/10.1016/j.jare.2019.12.004.

[9] A. Centrone, Infrared Imaging and Spectroscopy Beyond the Diffraction Limit, Annual Rev. Anal. Chem. 8 (1) (2015) 101–126.

[10] B. Knoll, F. Keilmann, Near-field probing of vibrational absorption for chemical microscopy, Nature 399 (6732) (1999) 134–137, https://doi.org/10.1038/20154.

[11] R.M. Stockle, Y.D. Suh, V. Deckert, R. Zenobi, S. Switzerland, Nanoscale chemical analysis by tip-enhanced Raman spectroscopy, Chem. Phys. Lett. 318 (1–3) (2000) 131–136, https://doi.org/10.1016/S0009-2614(99)01451-7.

[12] M.S. Anderson, Locally enhanced Raman spectroscopy with an atomic force microscope, Appl. Phys. Lett. 76 (21) (May 2000) 3130–3132, https://doi.org/10.1063/1.126546.

[13] S. Kenkel, S. Mittal, R. Bhargava, Closed-loop atomic force microscopy-infrared spectroscopic imaging for nanoscale molecular characterization, Nat. Commun. 11 (1) (Dec. 2020), https://doi.org/10.1038/s41467-020-17043-5.

[14] M. Brehm, A. Schliesser, F. Čajko, I. Tsukerman, F. Keilmann, Antenna-mediated back-scattering efficiency in infrared near-field microscopy, Opt. Express 16 (15) (2008) 11203, https://doi.org/10.1364/oe.16.011203.

[15] N. Mauser, A. Hartschuh, Tip-enhanced near-field optical microscopy, Chem. Soc. Rev. 43 (4) (2014) 1248–1262.

[16] N. Behr, M.B. Raschke, Optical antenna properties of scanning probe tips: Plasmonic light scattering, tip-sample coupling, and near-field enhancement, J. Phys. Chem. C 112 (10) (Mar. 2008) 3766–3773, https://doi.org/10.1021/jp7098009.

[17] G. Latour, L. Robinet, A. Dazzi, F. Portier, A. Deniset-Besseau, M.C. Schanne-Klein, Correlative nonlinear optical microscopy and infrared nanoscopy reveals collagen degradation in altered parchments, Sci. Rep. 6 (May 2016), https://doi.org/10.1038/srep26344.

[18] E. Lipiec, A. Wnętrzak, A. Chachaj-Brekiesz, W. Kwiatek, P. Dynarowicz-Latka, High-resolution label-free studies of molecular distribution and orientation in ultrathin, multicomponent model membranes with infrared nano-spectroscopy AFM-IR, J. Colloid Interface Sci. 542 (Apr. 2019) 347–354, https://doi.org/10.1016/j.jcis.2019.02.016.

[19] D. Partouche, J. Mathurin, A. Malabirade, S. Marco, C. Sandt, V. Arluison, A. Deniset-Besseau, S. Trepout, Correlative infrared nanospectroscopy and transmission electron microscopy to investigate nanometric amyloid fibrils: prospects and challenges, J. Microsc. 274 (1) (Apr. 2019) 23–31, https://doi.org/10.1111/jmi.12779.

[20] A. Deniset-Besseau, C.B. Prater, M.J. Virolle, A. Dazzi, Monitoring TriAcylGlycerols accumulation by atomic force microscopy based infrared spectroscopy in Streptomyces species for biodiesel applications, J. Phys. Chem. Lett. 5 (4) (Feb. 2014) 654–658, https://doi.org/10.1021/jz402393a.

[21] L. Bildstein, A. Deniset-Besseau, I. Pasini, C. Mazilier, Y.W. Keuong, A. Dazzi, N. Baghdadli, Discrete Nanoscale Distribution of Hair Lipids Fails to Provide Humidity Resistance, Anal. Chem. 92 (17) (2020) 11498–11504, https://doi.org/10.1021/acs.analchem.0c01043.

[22] J. Mathurin, E. Pancani, A. Deniset-Besseau, K. Kjoller, C.B. Prater, R. Gref, A. Dazzi, How to unravel the chemical structure and component localization of individual drug-loaded polymeric nanoparticles by using tapping AFM-IR, Analyst 143 (24) (Dec. 2018) 5940–5949, https://doi.org/10.1039/c8an01239c.

[23] M. Tuteja, M. Kang, C. Leal, A. Centrone, Nanoscale partitioning of paclitaxel in hybrid lipid-polymer membranes, Analyst 143 (16) (Aug. 2018) 3808–3813, https://doi.org/10.1039/c8an00838h.

[24] D. Święch, C. Paluszkiewicz, N. Piergies, E. Pięta, K. Kollbek, W.M. Kwiatek, Micro- and nanoscale spectroscopic investigations of threonine influence on the corrosion process of the modified fe surface by Cu nanoparticles, Materials (Basel) 13 (20) (Oct. 2020) 1–16, https://doi.org/10.3390/ma13204482.

[25] J. Mathurin, E. Dartois, T. Pino, C. Engrand, J. Duprat, A. Deniset-Besseau, F. Borondics, C. Sandt, A. Dazzi, Nanometre-scale infrared chemical imaging of organic matter in ultra-carbonaceous Antarctic micrometeorites (UCAMMs), Astron. Astrophys. 622 (2019) A160.

[26] A. Dazzi, C.B. Prater, Q. Hu, D. Bruce, J.F. Rabolt, C. Marcott, AFM-IR: Combining Atomic Force Microscopy and Infrared Spectroscopy for Nanoscale Chemical Characterization, Appl. Spectrosc. 66 (12) (2012) 1365–1384, https://doi.org/10.1366/12-06804.

[27] N. Piergies, E. Pięta, C. Paluszkiewicz, H. Domin, W.M. Kwiatek, Polarization effect in tip-enhanced infrared nanospectroscopy studies of the selective Y5 receptor antagonist Lu AA33810, Nano Res. 11 (8) (Aug. 2018) 4401–4411, https://doi.org/10.1007/s12274-018-2030-z.

[28] N. Piergies, M. Oćwieja, C. Paluszkiewicz, W.M. Kwiatek, Nanoparticle stabilizer as a determining factor of the drug/gold surface interaction: SERS and AFM-SEIRA studies, Appl. Surf. Sci. 537 (2021) 147897.

[29] N. Piergies, A. Dazzi, A. Deniset-Besseau, J. Mathurin, M. Oćwieja, C. Paluszkiewicz, W.M. Kwiatek, Nanoscale image of the drug/metal mono-layer interaction: Tapping AFM-IR investigations, Nano Res. 13 (4) (2020) 1020–1028.

[30] H.A. Pearce, N. Sheppard, Possible importance of a 'metal-surface selection rule' in the interpretation of the infrared spectra of molecules adsorbed on particulate metals; infrared spectra from ethylene chemisorbed on silica-supported metal catalysts, Surf. Sci. 59 (1) (1976) 205–217, https://doi.org/10.1016/0039-6028(76)90301-0.

[31] R.G. Greenler, D.R. Snider, D. Witt, R.S. Sorbello, The metal-surface selection rule for infrared spectra of molecules adsorbed on small metal particles, Surf. Sci. 118 (3) (1982) 415–428, https://doi.org/10.1016/0039-6028(82)90197-2.

[32] M. Osawa, K.I. Ataka, K. Yoshii, Y. Nishikawa, Surface-enhanced infrared spectroscopy: The origin of the absorption enhancement and band selection rule in the infrared spectra of molecules adsorbed on fine metal particles, Appl. Spectrosc. 47 (9) (1993) 1497–1502, https://doi.org/10.1366/0003702934067478.

[33] N. Piergies, M. Oćwieja, C. Paluszkiewicz, W.M. Kwiatek, Identification of erlotinib adsorption pattern onto silver nanoparticles: SERS studies, J. Raman Spectrosc. 49 (8) (Aug. 2018) 1265–1273, https://doi.org/10.1002/jrs.5384.

[34] N. Piergies, M. Oćwieja, C. Paluszkiewicz, W.M. Kwiatek, Spectroscopic insights into the effect of pH, temperature, and stabilizer on erlotinib adsorption behavior onto Ag nanosurface, Spectrochim. Acta - Part A Mol. Biomol. Spectrosc. 228 (2020) Mar, https://doi.org/10.1016/j.saa.2019.117737.

[35] J.I. Gersten, A. Nitzan, Photophysics and photochemistry near surfaces and small particles, Surf. Sci. 158 (1–3) (1985) 165–189, https://doi.org/10.1016/0039-6028(85)90293-6.

[36] A. Otto, I. Mrozek, H. Grabhorn, W. Akemann, Surface-enhanced Raman scattering, J. Phys.: Condens. Matter 4 (5) (1992) 1143–1212.

[37] M. Osawa, Dynamic Processes in Electrochemical Reactions Studied by Surface-Enhanced Infrared Absorption Spectroscopy (SEIRAS), Bulletin of the Chemical Society of Japan 70 (12) (1997) 2861–2880, https://doi.org/10.1246/bcsj.70.2861.

[38] C. Huck, F. Neubrech, J. Vogt, A. Toma, D. Gerbert, J. Katzmann, T. Hartling, A. Pucci, Surface-enhanced infrared spectroscopy using nanometer-sized gaps, ACS Nano 8 (5) (May 2014) 4908–4914, https://doi.org/10.1021/nn500903v.

[39] J. Kundu, F. Le, P. Nordlander, N.J. Halas, Surface enhanced infrared absorption (SEIRA) spectroscopy on nanoshell aggregate substrates, Chem. Phys. Lett. 452 (1–3) (Feb. 2008) 115–119, https://doi.org/10.1016/j.cplett.2007.12.042.

[40] J. Krajczewski, K. Kołątaj, A. Kudelski, Plasmonic nanoparticles in chemical analysis, RSC Adv. 7 (28) (2017) 17559–17576.

[41] H. Ghosh, T. Bürgi, Mapping Infrared Enhancement around Gold Nanoparticles Using Polyelectrolytes, J. Phys. Chem. C 121 (4) (Feb. 2017) 2355–2363, https://doi.org/10.1021/acs.jpcc.6b10613.

[42] Z. Zhu, T. Zhu, Z. Liu, Raman scattering enhancement contributed from individual gold nanoparticles and interparticle coupling, Nanotechnology 15 (3) (Mar. 2004) 357–364, https://doi.org/10.1088/0957-4484/15/3/022.

[43] R.J. Cersosimo, Gefitinib: An adverse effects profile, Expert Opinion on Drug Safety 5 (3) (May 2006) 469–479, https://doi.org/10.1517/14740338.5.3.469.

[44] P.C. Lee, D. Meisel, Adsorption and surface-enhanced Raman of dyes on silver and gold sols, J. Phys. Chem. 86 (17) (1982) 3391–3395, https://doi.org/10.1021/j100214a025.

[45] J. Turkevich, G. Garton, P.C. Stevenson, The color of colloidal gold, J. Colloid Sci. 9 (1) (1954) 26–35, https://doi.org/10.1016/0095-8522(54)90070-7.

[46] J. Turkevich, Colloidal gold. Part II, Gold Bull. 18 (4) (1985) 125–131, https://doi.org/10.1007/bf03214694.

[47] E. Isac Paulraj, S. Muthu, Molecular structure analysis and spectroscopic characterization of 5-ethyl-5-phenyl-1,3-diazinane-4,6-dione with experimental (FT-IR and FT-Raman) techniques and quantum chemical calculations, Spectrochim. Acta - Part A Mol. Biomol. Spectrosc. 106 (2013) 310–320, https://doi.org/10.1016/j.saa.2013.01.048.

[48] M. Oćwieja, Z. Adamczyk, M. Morga, A. Michna, High density silver nanoparticle monolayers produced by colloid self-assembly on polyelectrolyte supporting layers, J. Colloid Interface Sci. 364 (1) (2011) 39–48, https://doi.org/10.1016/j.jcis.2011.07.059.

[49] M. Morga, Z. Adamczyk, Monolayers of cationic polyelectrolytes on mica - Electrokinetic studies, J. Colloid Interface Sci. 407 (2013) 196–204, https://doi.org/10.1016/j.jcis.2013.05.069.

[50] N. Piergies, E. Proniewicz, Y. Kim, L.M. Proniewicz, Interaction of N-benzylamino (boronphenyl)methylphosphonic acid analogs with the gold colloidal surface

under different concentration and pH conditions, Journal of Raman Spectroscopy 45 (7) (2014) 581–590, https://doi.org/10.1002/jrs.4505.
[51] A.T.N. Lam, J. Yoon, E.-O. Ganbold, D.K. Singh, D. Kim, K.-H. Cho, S.Y. Lee, J. Choo, K. Lee, S.-W. Joo, Colloidal gold nanoparticle conjugates of gefitinib, Colloids and Surfaces B: Biointerfaces 123 (2014) 61–67.
[52] Y. Qi, Y. Hu, M. Xie, D. Xing, H. Gu, Adsorption of aniline on silver mirror studied by surface-enhanced Raman scattering spectroscopy and density functional theory calculations, J. Raman Spectrosc. 42 (6) (Jun. 2011) 1287–1293, https://doi.org/10.1002/jrs.2864.
[53] S. SenGupta, N. Maiti, R. Chadha, S. Kapoor, Conformational analysis of morpholine studied using Raman spectroscopy and density functional theoretical calculations, Chem. Phys. Lett. 639 (Oct. 2015) 1–6, https://doi.org/10.1016/j.cplett.2015.09.003.
[54] M. Xie, G. Zhu, Y. Hu, H. Gu, Conformations of morpholine in liquid and adsorbed on gold nanoparticles explored by Raman spectroscopy and theoretical calculations, J. Phys. Chem. C 115 (42) (Oct. 2011) 20596–20602, https://doi.org/10.1021/jp206544a.
[55] N. Piergies, E. Proniewicz, Y. Ozaki, Y. Kim, L.M. Proniewicz, Influence of substituent type and position on the adsorption mechanism of phenylboronic acids: Infrared, raman, and surface-enhanced raman spectroscopy studies, J. Phys. Chem. A 117 (27) (Jul. 2013) 5693–5705, https://doi.org/10.1021/jp404184x.
[56] G. Ilango, M. Arivazhagan, J.J. Prince, V. Balachandran, FTIR and FT-Raman spectral investigation of 2-chloro-1,3-dibromo-5- fluorobenzene, Indian J. Pure Appl. Phys. 46 (10) (2008) 698–701.
[57] N. Piergies, C. Paluszkiewicz, W.M. Kwiatek, Vibrational fingerprint of erlotinib: Ftir, rs, and DFT studies, J. Spectrosc. 2019 (2019) 1–10.
[58] A.T.N. Lam, J. Yoon, E.-O. Ganbold, D.K. Singh, D. Kim, K.-H. Cho, S.J. Son, J. Choo, S.Y. Lee, S. Kim, S. Joo, Adsorption and desorption of tyrosine kinase inhibitor erlotinib on gold nanoparticles, J. Colloid Interface Sci. 425 (Jul. 2014) 96–101, https://doi.org/10.1016/j.jcis.2014.03.032.
[59] M. Moskovits, J.S. Suh, Surface selection rules for surface-enhanced Raman spectroscopy: Calculations and application to the surface-enhanced Raman spectrum of phthalazine on silver, J. Phys. Chem. 88 (23) (1984) 5526–5530, https://doi.org/10.1021/j150667a013.
[60] M. Moskovits, Surface-enhanced spectroscopy, Rev. Mod. Phys. 57 (785) (1985) 783–826, https://doi.org/10.1103/RevModPhys.57.783.
[61] S. Yoo, Q.-H. Park, Effective permittivity for resonant plasmonic nanoparticle systems via dressed polarizability, Opt. Express 20 (15) (2012) 16480, https://doi.org/10.1364/oe.20.016480.
[62] M. Rycenga, C.M. Cobley, J. Zeng, W. Li, C.H. Moran, Q. Zhang, D. Qin, Y. Xia, Controlling the synthesis and assembly of silver nanostructures for plasmonic applications, Chem. Rev. 111 (6) (2011) 3669–3712, https://doi.org/10.1021/cr100275d.
[63] H.-L. Wang, E.-M. You, R. Panneerselvam, S.-Y. Ding, Z.-Q. Tian, Advances of surface-enhanced Raman and IR spectroscopies: from nano/microstructures to macro-optical design, Light Sci Appl 10 (1) (2021).
[64] H. Ghosh, T. Bürgi, Adsorption of gold and silver nanoparticles on polyelectrolyte layers and growth of polyelectrolyte multilayers: An in situ ATR-IR study, J. Phys. Chem. C 117 (50) (2013) 26652–26658, https://doi.org/10.1021/jp409241t.
[65] F. Lu, M. Jin, M.A. Belkin, Tip-enhanced infrared nanospectroscopy via molecular expansion force detection, Nat. Photonics 8 (4) (2014) 307–312, https://doi.org/10.1038/nphoton.2013.373.
[66] V.P. Drachev, S.V. Perminov, S.G. Rautian, Optics of metal nanoparticle aggregates with light induced motion, Opt. Express 15 (14) (2007) 8639, https://doi.org/10.1364/oe.15.008639.
[67] K. Danielsson, J.A. Gallego-Urrea, M. Hassellov, S. Gustafsson, C.M. Jonsson, Influence of organic molecules on the aggregation of TiO2 nanoparticles in acidic conditions, J Nanopart Res 19 (4) (2017).
[68] J.J. Mock, S.M. Norton, S.Y. Chen, A.A. Lazarides, D.R. Smith, Electromagnetic Enhancement Effect Caused by Aggregation on SERS-Active Gold Nanoparticles, Plasmonics 6 (1) (2011) 113–124, https://doi.org/10.1007/s11468-010-9176-1.
[69] K. Kim, K.L. Kim, H.B. Lee, K.S. Shin, Surface-enhanced Raman scattering on aggregates of platinum nanoparticles with definite size, J. Phys. Chem. C 114 (43) (2010) 18679–18685, https://doi.org/10.1021/jp1078532.
[70] S. Mehigan, C.A. Smyth, E.M. McCabe, Bridging the gap between SERS enhancement and reproducibility by salt aggregated silver nanoparticles, Nanomater. Nanotechnol. 5 (1) (2015) 1–6, https://doi.org/10.5772/60125.